Deformation-activated polarization-selective negative group velocity in rectangularly-arranged fiber-reinforced soft composite

Deformation-activated polarization-selective negative group velocity in rectangularly-arranged fiber-reinforced soft composite

Qi Yao[a*], Stephan Rudykh[a,b*]

[a] *Department of Mechanical Engineering, University of Wisconsin– Madison, Madison, WI 53706, United States*

[b] *School of Mathematical and Statistical Sciences, University of Galway, University Road, Galway, Ireland*

* Corresponding author. E-mail address: qyao34@wisc.edu (Q. Yao).

* Corresponding author. E-mail address: stephan.rudykh@universityofgalway.ie (S. Rudykh).

Abstract

This paper demonstrates the deformation-activated negative group velocity (NGV) state in soft fiber-reinforced composites (soft FCs). We exhibit the mechanism of inducing the NGV state in the vicinity of buckling. Based on extensive simulations, we construct a map of NGV intervals versus deformation level and fiber spacing ratio, revealing clear trends and tunable behavior. In the transition region of buckling direction, NGV states can be selectively activated for shear waves with different polarizations. The presence and order of NGV polarizations are found to correlate with the direction of post-buckling fiber morphology. NGV states in both polarizations indicate non-principal, helical buckling patterns and complex evolutions. The relative width of NGV intervals of two polarizations mirrors the magnitude of helical deformation in each direction. These findings suggest NGV behavior as a predictive indicator for post-buckling configurations. This work offers a new pathway for understanding NGV states in soft FCs, with potential applications in reconfigurable materials.

Keywords: Acoustic metamaterial, Elastic instabilities, Shear waves, Dispersion relations, Negative group velocity

1 Introduction

Acoustic metamaterial is a category of matters that allows us to manipulate the ways elastic waves propagate. A variety of novel functionalities and unusual properties has been developed in these materials, including negative refractive index (Bongard et al., 2010; Wang et al., 2021),

negative modulus and density (Lee and Wright, 2016; Mokhtari et al., 2019), bandgap (Galich et al., 2017a; Gao et al., 2021; Zhang et al., 2018), negative group velocities (Carcaterra et al., 2019; Han and Liu, 2003), cloaking (Cheng et al., 2008), acoustic diode (Li et al., 2011; Sun et al., 2012), and others. These unexpected properties originate from their predesigned microstructures, constitutive relations, and stimuli-induced behavior. Therefore, developing desired functionalities requires us to study the behavior of metamaterials excited by various stimuli. Soft metamaterials are especially well-suited for developing tunable acoustic properties, as they can respond to various stimuli and undergo large, recoverable deformation (Dorfmann and Ogden, 2010; Galich et al., 2017b; Galich and Rudykh, 2017; Gao et al., 2021, 2019; Shan et al., 2014; Shmuel et al., 2012; Wang et al., 2014; Yerrapragada et al., 2023).

For elastic waves, the energy is proportional to the momentum (Kittel, 2005). However, a local minimum energy status can be induced at finite momentum. This unusual dispersion relation has been observed in liquid Hlium-4 (Beauvois et al., 2018; Henshaw and Woods, 1961; Woods, 1965) and 2D Hliqum-3 (Godfrin et al., 2012) at low temperatures. Furthermore, the appearance of local minimum energy also induces a region of negative slope ($\partial f/\partial \bar{k}_3 < 0$) on the dispersion curves. The state where group velocity $v_{gr} = \partial f/\partial \bar{k}_3 < 0$ is regarded as the negative group velocity state (NGV state). This state characterized by the opposite direction of phase and group velocities can give rise to the backward wave and lead to negative refraction (Chen et al., 2021; García-Chocano et al., 2014; Smith et al., 2004; Wang et al., 2022; Zhu et al., 2014).

Until recently, negative group velocity has been observed in a variety of soft metamaterials. Slesarenko et al. (2018) first analyzed the appearance of NGV states in soft laminates and provided a map of interval width over parameter space. Arora et al. (2022) further demonstrated the existence of NGV in stable regions of Gent laminates and achieved the interval with extended width. Galich et al. (2018) pioneered the study of dispersion relations in soft fiber-reinforced composites (FCs), reporting negative dispersion found negative dispersions in both shear wave polarizations and suggesting its connection to fiber buckling into helical shapes. Wang et al. (2026, 2022) and Chen et al. (2021) conducted detailed continuous studies on activating acoustic backward waves through beyond-nearest-neighbor between lattices. Together, these studies highlight the potential of NGV states to induce tunable acoustic

functionalities in soft materials. Beyond wave manipulation, the NGV state potentially serves as a predictive marker for buckling, as it often precedes the appearance of zero-eigenfrequency (Slesarenko et al., 2018). Thus, the manipulation of buckling behavior can reverse influence the NGV state. To improve the instability prediction and functionality design, it is essential to understand the interplay between NGV and buckling behavior.

This paper presents our study into the negative group velocity states in soft fiber-reinforced composites with rectangular in-plane fiber arrangements. We analyze the appearance of NGV for transverse/shear waves (S-waves) with distinct polarizations propagating along the fiber axis. Compressive loading applied parallel to the fiber induces the NGV state prior to the occurrence of instability that activates the microstructure transformation. By considering FCs with adjustable in-plane periodicity, we extend previous studies on negative dispersion relations to enable dual-polarization NGV states that can be tuned by deformation. Furthermore, we can provide a comprehensive map of the trends in NGV interval as functions of spacing ratio and shear modulus contrast. Consequently, we can further explore the possibility that NGV state can serve as a precursor for post-buckling fiber morphology, as it is our long-term effort in achieving novel patterns for advanced functionalities.

This paper is organized as follows: in Section 3.1, we present the mechanism for activating NGV states in FCs; in Section 3.2, we construct a comprehensive map of NGV intervals with respect to spacing ratio/fiber arrangement and further examine the connection between intervals and buckled fiber morphologies; in Section 3.3, we analyzed the influence of varying initial shear modulus contrasts on the tunability and accessibility of NGV states, further expanding the design space.

2 Material definition and modeling

Consider the compression of a representative soft fiber-reinforced composite (FC) with varying in-plane periodicity in the three-dimensional view as shown by Fig. 1. FC contains two distinct phases, including stiff fiber with circular cross-section ($r = m$) and soft matrix ($r = f$) highlighted by black and white, respectively. Without a specific statement, the parameters and fields for two phases are all represented by $(\cdot)^{(r)}$. The volume fraction of fiber $c^{(f)}$ is set to

be much smaller than $c^{(m)}$. The initial shear modulus contrast $k_\mu = \mu^{(f)}/\mu^{(m)}$ is a high value to ensure the stiffness of fiber over matrix. Assuming two phases to be incompressible, the volume fractions own relationship that $c^{(m)} = 1 - c^{(f)}$. In Fig. 1, a coordinate system is attached to FC. $\mathbf{e}_i\{i = 1,2,3\}$ are base vectors. In the reference configuration $\mathbf{\Omega}_0$, the fibers are inserted as an array along $\mathbf{e}_1$ and $\mathbf{e}_2$ every distance W and D, respectively. Thus, the dimension of one unit cell is $W \times D$. The fiber radius is $R = \sqrt{WDc^{(f)}/\pi}$ under the constraint of unit cell dimension. Moreover, the contrast between D and W is defined as spacing ratio $\xi = D/W$. The height of FC must be significantly larger than D and W.

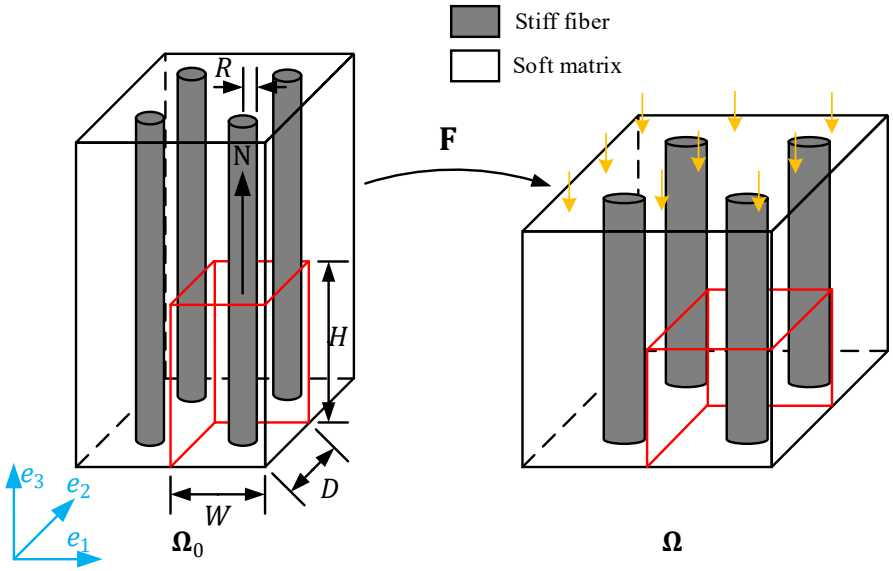

Fig. 1 Schematic of fiber-reinforced composite (FC) with in-plane periodicity under uniaxial compression along $\mathbf{e}_3$ from undeformed configuration to deformed configuration. A single unit cell for analysis is highlighted. As specified, the acoustic wave propagates along the fiber orientation.

The constitutive behavior of phases is defined by the neo-Hookean strain energy density function (SEDF)

$$W^{(r)}\left(\mathbf{F}^{(r)}\right) = \frac{\mu^{(r)}}{2}\left(I_1^{(r)} - 3\right) + \frac{\kappa^{(r)}}{2}\left(J^{(r)} - 1\right)^2, \tag{1}$$

where $\mu^{(r)}$ and $\kappa^{(r)}$ represents the shear modulus and bulk modulus of phase r, respectively; $\mathbf{F}^{(r)}$ denotes the deformation gradient tensor; $J^{(r)} \equiv \det \mathbf{F}^{(r)}$; $I_1^{(r)} = \mathrm{tr}\left(\mathbf{F}^{(r)T}\mathbf{F}^{(r)}\right)$. To ensure the incompressible of phases, a high bulk-to-shear modulus ratio, $\kappa^{(r)}/\mu^{(r)} = 1000$ is set. As shown by Fig. 1, FC undergoes the uniaxial compression defined by the following

macroscopic deformation gradient $\bar{\mathbf{F}}$

$$\bar{\mathbf{F}} = \lambda^{-1/2}\boldsymbol{e}_1\otimes\boldsymbol{e}_1 + \lambda^{-1/2}\boldsymbol{e}_2\otimes\boldsymbol{e}_2 + \lambda\boldsymbol{e}_3\otimes\boldsymbol{e}_3, \tag{2}$$

where λ is the macroscopic stretch ratio applied along $\boldsymbol{e}_3$.

To study the elastic wave propagation, small amplitude displacement is superimposed onto the finitely compressed FC. The incremental equation of displacement is

$$\mathrm{Div}\dot{\mathbf{P}} = \rho_0 \frac{D^2\dot{\mathbf{u}}}{Dt^2}, \tag{3}$$

where $D^2(\ )/Dt^2$ represents the material time derivative; Div is the divergence operator with respect to the position vector $\mathbf{X}$ in $\boldsymbol{\Omega}_0$; ρ_0 is the initial material density; $\dot{\mathbf{u}}$ is the infinitesimal incremental displacement; $\dot{\mathbf{P}}$ is incremental change in the first Piola-Kirchhoff stress and defined as a linearized constitutive relation $\dot{\mathbf{P}} = \mathbb{C}\dot{\mathbf{F}}$ with $\mathbb{C} = \frac{\partial^2 W(\mathbf{X},\mathbf{F})}{\partial\mathbf{F}\partial\mathbf{F}}$ representing tensor of elastic moduli and $\dot{\mathbf{F}} = \frac{\partial\dot{\mathbf{u}}}{\partial\mathbf{X}}$ denoting the incremental deformation gradient. In the periodic FC, the superimposed small amplitude displacement is the Bloch wave

$$\dot{\mathbf{u}}(\mathbf{X},t) = \mathbf{U}(\mathbf{X})\exp[i(\mathbf{K}\cdot\mathbf{X} - \omega t)], \tag{4}$$

where ω is the angular frequency, $\mathbf{K} = K_1\boldsymbol{e}_1 + K_2\boldsymbol{e}_2 + K_3\boldsymbol{e}_3$ is the Bloch wave vector in the $\boldsymbol{\Omega}_0$, i is the complex number unit, and $\mathbf{U}(\mathbf{X})$ is a periodic function that satisfies the periodicity condition $\mathbf{U}(\mathbf{X}+\mathbf{R}) = \mathbf{U}(\mathbf{X})e^{i\mathbf{K}\cdot\mathbf{R}}$. $\mathbf{R} = R_1W\boldsymbol{e}_1 + R_2D\boldsymbol{e}_2 + R_3H\boldsymbol{e}_3$ is an arbitrary vector with integer coordinates R_1, R_2, R_3that denotes the spatial periodicity in $\boldsymbol{\Omega}_0$. Focusing on wave propagating along $\boldsymbol{e}_3$, the Bloch wave vector reduces to $\mathbf{K} = K_3\boldsymbol{e}_3$. The Bloch wave vector $\mathbf{k}$ in the deformed configuration is calculated by $\mathbf{k} = \mathbf{F}^{-T}\mathbf{K}$. The wavenumber is normalized as $\bar{k}_3 = k_3W/(2\pi)$.

To study the dispersion relationship of FC, a unit cell shown in Fig. 1 is studied in simulation. The model of unit cell computes the dispersion curves during deformation. Wave frequencies over wavenumber $\bar{k}_3$ are computed to plot the dispersion curve $f = \omega(\bar{k}_3)/(2\pi)$. The corresponding group velocity curve is $v_{gr} = \partial f/\partial\bar{k}_3$. According to the previous study (Galich et al., 2018), FC in rectangular arrangement sees a separation of shear wave (S-wave) with different polarizations. Thus, the group velocities for waves with different polarizations must be analyzed. Moreover, FC loses stability on macro- or microscopic range upon a certain deformation level (say critical stretch λ^{cr}), which depends on the geometric and material

parameters (Bertoldi and Lopez-Pamies, 2012; Geymonat et al., 1993; Rudykh and Debotton, 2012; Triantafyllidis and Maker, 1985). The macro-instability appears on a scope that is much larger than the characteristic sizes of its microstructure with critical wave number $\bar{k}_3^{cr} \to 0$. However, the micro-instability emerges in length approximate to the dimension of unit cell with $\bar{k}_3^{cr}$ significantly larger than zero. The emergence of instability is characterized by the wave frequency $f \to 0$ on a dispersion curve. The proposed research (Arora et al., 2022a, 2020; Galich et al., 2018; Li et al., 2018) reveals that micro-instability enables microstructure transformation and bending of dispersion curves while macro-instability with $\bar{k}_3^{cr} \to 0$ cannot induce a NGV state. Thus, this paper focuses on variation of dispersion relations and occurrence of negative group velocity in micro-instability domain. For FC in a rectangular arrangement, the instability appears in a direction-altering behavior (Arora et al., 2022a; Galich et al., 2018) through adjusting the spacing ratio. Except for computing dispersion relationship and the group velocity, this model also analyzes instability points, including critical stretch ratio, critical wavenumber, and buckling orientation (See Appendix A for more details on simulations).

3 Results

3.1 Mechanism of deformation activated NGV for polarized S-wave

To analyze the development of dispersion curves versus deformation and thus observe the occurrence of the NGV state, two representative examples are plotted in Fig. 2 (a) and (b) with $c^{(f)} = 0.05,\ k_\mu = 80,\ \xi = 2$ and $c^{(f)} = 0.05,\ k_\mu = 15, \xi = 2$, respectively. Fig. 2 (a) and (b) display the frequency and group velocity as functions of normalized wavenumber. The instability analysis indicates that these two cases should buckle in $\boldsymbol{e}_1$. Due to the S-wave separation (Galich et al., 2018), wave frequencies correspond to eigenmodes with divergent polarizations. The dispersion curves and group velocity curves are separated into S-waves polarized in u_1 $(f_{u_1}, v_{u_1,gr})$ and those polarized in u_2 $(f_{u_2}, v_{u_2,gr})$. A gray region covers the area where group velocity is negative. Fig. 2 (c) includes S-wave modes that change with deformation level with wavenumber $\bar{k}_3 = 0.25$ in FC with $c^{(f)} = 0.05,\ k_\mu = 15,\ \xi = 2$. The modes are plotted for the undeformed ($\lambda = 1$), moderately deformed ($\lambda = 0.9, 0.8$), and NGV activated ($\lambda = 0.75261$) states.

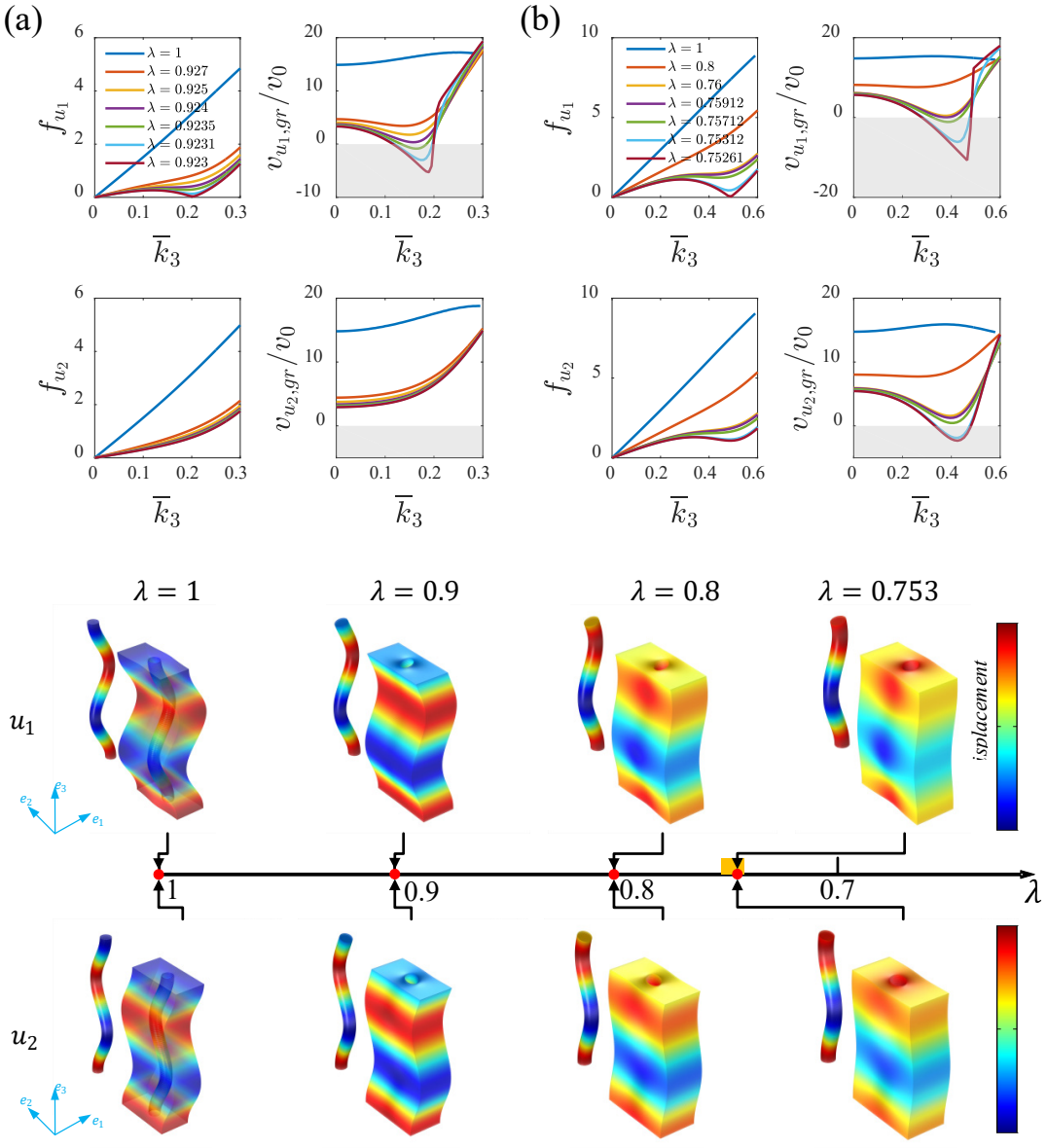

Fig. 2 Occurrence of negative group velocity state in both polarizations. Dispersion relation $f(\bar{k}_3)$ and group velocity $v_{gr}(\bar{k}_3)$ change versus deformation for $c^{(f)} = 0.05, k_\mu = 80, \xi = 2$ (a) and $c^{(f)} = 0.05, k_\mu = 15, \xi = 2$ (b). (c) S-wave modes with $\bar{k}_3 = 0.25, c^{(f)} = 0.05, k_\mu = 15, \xi = 2$ at λ = 1,0.9,0.8, and 0.75261.

Figure 2 primarily shows that the deformation applied onto FC enables the tuning of S-wave dispersion relations. From undeformed ($\lambda = 1$) to compressed (for example, at $\lambda = 0.8$ in Fig. 2 (a)) state, the initially linear relation turns into a non-linear one. The contraction effectively affects the dispersion relation within a wavenumber interval containing the critical wavenumber $\bar{k}_3^{cr}$, as previously observed (Arora et al., 2022b). For intervals $0.15 \leq \bar{k}_3 \leq 0.25$ and $0.3 \leq \bar{k}_3 \leq 0.6$ in Fig. 2 (a) and (b), respectively, the dispersion curves are significantly tuned in both values and slopes. Outside of this interval over critical wavenumber,

the influence of compression becomes weaker. For $\bar{k}_3 \leq 0.1$, FC from Fig. 2 (b) shows a dispersion relation less affected by the deformation. As deformation level increases, taking $\lambda = 0.924$ in Fig. 2 (a) as an instance, the dispersion curves from a plateau in the neighbor interval of critical wavenumber, in which the group velocity turns zero ($v_{gr} = 0$). When deformation increases further, the slopes of the curve enter the negative domain and the NGV ($v_{gr} < 0$) appears while frequencies remain positive ($f > 0$). This NGV state can be activated and tuned through deformation. From $\lambda = 0.924$ to 0.923, for example, the range of wavenumber $\Delta\bar{k}_{ngv}$ where NGV appears to expand.

One significant difference between FCs with $k_\mu = 15$ and $k_\mu = 80$ is the presence of NGV for S-waves with different polarizations. At $k_\mu = 80$, FC exhibits NGV state purely for S-wave polarized in u_1. On the other hand, $k_\mu = 15$ enables NGV for S-wave in both polarizations. Here and thereafter, they are named as single-polarization and double-polarization NGV, respectively. This difference can be attributed to the distinct buckling behavior between these two cases. The FC with $k_\mu = 15$ is predicted to buckle in $\boldsymbol{e}_1$. However, published research (Arora et al., 2022a) shows that it buckles in a non-principal direction, which is a hybrid instability mode. This progress drives the dispersion curve f_{u_1} and f_{u_2} to bend toward zero. Upon $\lambda = 0.75912$, f_{u_1} curve initially forms a zero-slope state. At $\lambda = 0.75712$, f_{u_2} curve also approaches a zero-group-velocity state. Simultaneously, $\Delta\bar{k}_{ngv}$ for waves with u_1 polarization is expanding. Further compression enables NGV for both polarizations. In the case with $k_\mu = 80$, FC singly buckles in $\boldsymbol{e}_1$, the polarization in which the NGV state occurs. In summary, the buckling behavior with varying directions can provide insight into tunable "polarization-selective" negative group velocity. The NGV state reversely forecasts the instability behavior by predicting its buckling direction. This tunable NGV state versus spacing ratio is further studied in the following subsections.

Figure 2 (c) illustrates that the high-level amplitude of displacement appears in the matrix when the group velocity is positive in the undeformed state ($\lambda = 1$). Under further compression, see $\lambda = 0.9$ and 0.8, the displacement in the matrix reduces relative to that in fiber. When the group velocity turns negative for waves in both polarizations, the deformation (see $\lambda = 0.75261$) approaches instability, demonstrating the reliance of the NGV state on the instability. It has been shown that the instability of FC is determined by the buckling of fiber,

which induces the concentration of displacement in that phase. Since the instability analysis predicts the non-principal buckling of FC with $k_\mu = 15$, the negative group velocity state is observed for waves with two polarizations.

3.2 Polarization-selective NGV versus spacing ratio

See the negative group velocity for S-waves with different polarizations in Fig. 2, several new variables are defined to facilitate analysis of the negative group velocity interval. λ^{NGV-u_1} (onset stretch for u_1) and λ^{NGV-u_2} (onset stretch for u_2) denote the onset stretch of the NGV state in waves with u_1 and u_2 polarization, respectively. λ^{NGV-e} (disappearance stretch) is the ending stretch of the NGV interval. Particularly, the ending stretch of the NGV interval is the same as the critical stretch in the study conducted by this paper. Here and thereafter, λ^{NGV-u_1}, λ^{NGV-u_2}, and λ^{NGV-e} are respectively denoted by left half-filled, upper half-filled, and void markers, unless stated otherwise. To measure the widths of different NGV intervals, three variables are defined as $\Delta\varepsilon^{NGV-u_1} = \lambda^{NGV-u_1} - \lambda^{NGV-e}$ (u_1 width), $\Delta\varepsilon^{NGV-u_2} = \lambda^{NGV-u_2} - \lambda^{NGV-e}$ (u_2 width), and $\Delta\varepsilon^{NGV} = \max\{\Delta\varepsilon^{NGV-u_1}, \Delta\varepsilon^{NGV-u_2}\}$ (total width), representing the width of the NGV interval for waves with u_1 polarization, width of the NGV interval for waves with u_2 polarization, and total width of the NGV interval, respectively. Distinct from $\Delta\varepsilon^{NGV-u_1}$ (left half-filled maker) and $\Delta\varepsilon^{NGV-u_2}$ (upper half-filled maker), $\Delta\varepsilon^{NGV}$ is covered by a gray background. In Fig. 3 (a) and (b), these variables are shown as functions of spacing ratio with $c^{(f)} = 0.05$ and $k_\mu = 80$.

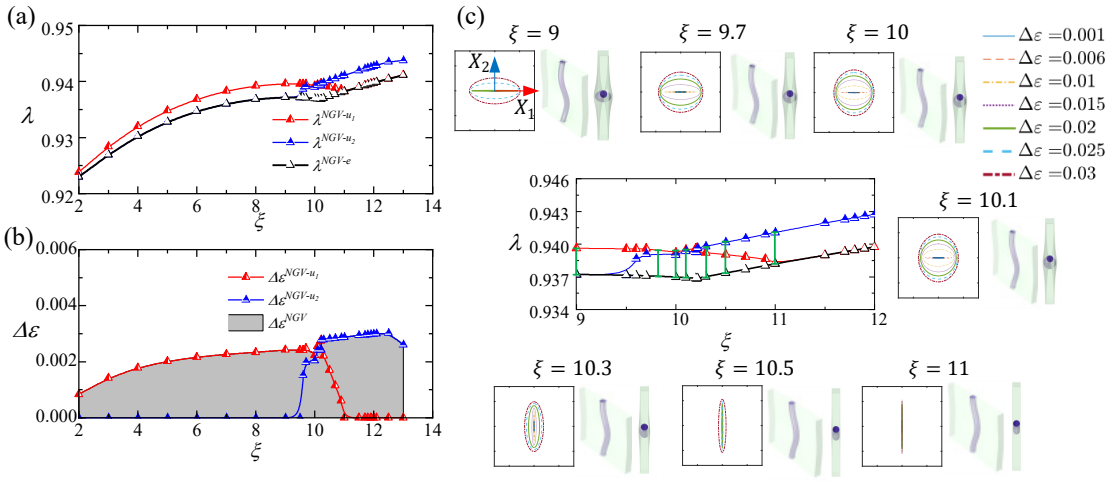

Fig. 3 Evolution of NGV interval and corresponding post-buckling fiber morphology versus spacing ratio in FCs with $c^{(f)} = 0.05$ and $k_\mu = 80$. (a) Changes of λ^{NGV-u_1}, λ^{NGV-u_2}, and λ^{NGV-e} versus spacing ratio. (b) Variation of u_1, u_2 and total width of NGV interval. (C) NGV intervals and corresponding fiber morphology evolution at a range of spacing ratios close to the transition point of buckling direction. The spacing ratios included are $\xi = 9, 9.7, 10, 10.1, 10.3, 10.5, 11$. A pair of axes X_1 and X_2 is attached to the center of fiber axis with X_1 parallel to $\boldsymbol{e}_1$ and X_2 parallel to $\boldsymbol{e}_2$.

Figure 3 shows the spacing ratio into three major intervals that contain NGV states with highly divergent properties. In $2 \leq \xi \leq 9.5$, onset stretch for u_1 and disappearance stretch increase and as do u_1 width and total width. According to the instability analysis, FC buckles in $\boldsymbol{e}_1$. Thus, this behavior drives the dispersion curve section for waves with u_1 polarization to bend toward zero, forming the NGV interval for waves in the same polarization ($\Delta\varepsilon^{NGV-u_1} = \Delta\varepsilon^{NGV}$, $\Delta\varepsilon^{NGV-u_2} = 0$). A similar phenomenon appears in $11 \leq \xi \leq 13$. At the spacing ratio from this interval, the buckling direction is $\boldsymbol{e}_2$. Hence, NGV state for waves with u_2 polarization is detected ($\Delta\varepsilon^{NGV-u_2} = \Delta\varepsilon^{NGV}$, $\Delta\varepsilon^{NGV-u_1} = 0$). Increasing the spacing ratio results in an overall extension of NGV interval (see rising $\Delta\varepsilon^{NGV}$ in Fig. 3). At high spacing ratio, the bending of dispersion curves appears at a small compression level. Then, the increase in deformation level for the onset of NGV state is more rapid than the rise of the disappearance stretch. Moreover, the disappearance stretch, which is the same as the critical stretch, exhibits an overall increasing trend in these two intervals. When the spacing ratio is increasing, the stability of FC is weakened, and smaller deformation is required to activate instability.

Aside from the similarities in these two intervals of spacing ratios, the intriguing variation in NGV for $9.5 \leq \xi \leq 11$ contains more information. From 9.5 to 10, the NGV state for waves with u_2 polarization emerges and rapidly increases to the same magnitude as u_1 width ($\Delta\varepsilon^{NGV-u_1} \approx \Delta\varepsilon^{NGV-u_2} \approx \Delta\varepsilon^{NGV}$). In a small interval $10 \leq \xi \leq 10.3$, the approximate onset stretches for u_1 and u_2 suggest that the dispersion curves for both polarizations bend into negative slopes almost at the same deformation level. Around $\xi = 10.2$, onset stretches for u_1 and u_2 jump simultaneously to a higher level, extending total width. From $\xi = 10.3$ to $\xi = 11$, u_1 width rapidly decreases to zero and the NGV interval starts from the NGV for waves with u_2 polarization ($\lambda^{NGV-u_2} > \lambda^{NGV-u_1}$). The onset stretch curve for u_1 decreases from

the peak and merges into the disappearance stretch. The onset stretch for u_2 , however, diverge from the disappearance stretch and continuously increase. Then, only the NGV state for waves with u_2 polarization is observed for $\xi \geq 11$. In the transition region of buckling direction, the combinative utilization of spacing ratio and deformation level allows for the tuning of NGV states in a wide range.

The published research reveals that non-principal buckling direction appears in the transition region (Arora et al., 2022a). Thus, this non-principal buckling tendency induces the negative group velocity for S-waves with two polarizations. In an alternative expression, the simultaneous onset of negative group velocity for S-waves with different polarizations shows the ability to serve as a measure for identifying the transition region ("instability forecasting"). The polarization that undergoes negative group velocity first remarks the section for primary buckling direction ($\lambda^{NGV-u_1} > \lambda^{NGV-u_2}, \xi < 10.2$) and the section for secondary buckling direction ($\lambda^{NGV-u_1} < \lambda^{NGV-u_2}, \xi > 10.2$) in the transition region. Therefore, the transition point of buckling direction, which is $\xi = 10.2$ predicted by the instability analysis, can be identified by a simultaneous onset of NGV state for two polarizations, say $\lambda^{NGV-u_2} \approx \lambda^{NGV-u_1}$.

We note that the strong correlation between NGV state and buckling fiber morphologies can be observed. This also indicates the "instability forecasting" property of the NGV state. To further explore the relationship between NGV interval structure and fiber morphologies, we included the fiber central curve contour (FCCC, see our previous work) versus post-buckling deformation $\Delta\varepsilon = \lambda^{cr} - \lambda$ and buckled pattern at $\Delta\varepsilon = 0.03$ for a series of spacing ratios in Fig. 3 (c). For the spacing ratios significantly different from transition point, such as $\xi = 9$ and 11, NGV state for single polarization appears, and the fiber majorly buckles in the orientation along the polarization. When the spacing ratio approaches the transition point for the lower side ($\xi < \xi^t,\ \xi \to \xi^t$), the NGV states for shear waves polarized in u_1 appear first. On the other hand, the buckled fiber initially bends along $\boldsymbol{e}_1$. This can be observed at $\xi = 9.7, 10,$ and 10.1. Furthermore, the onset of NGV states for u_2 waves forecast the buckling of fiber in the second direction. From $\xi = 9.7$ to 10.1, λ^{NGV-u_2} increase and also for the secondary buckling of fiber occurs at an earlier stage. For spacing ratio approximate to the transition point but higher than it $\xi > \xi^t$, we can also observe the secondary buckling and the appearance of NGV state for waves with the other polarization. See $\xi = 10.3,$ and 10.5, the

fiber initially buckles in $\boldsymbol{e}_2$ and we have $\lambda^{NGV-u_2} > \lambda^{NGV-u_1}$. When the spacing ratio increase from 10.3 to 10.5, λ^{NGV-u_1} move close to λ^{NGV-e}. The extension of fiber along X_1 appears at higher strain level. At $\Delta\varepsilon = 0.03$, the X_1 magnitude of FCCC for $\xi = 10.5$ is smaller than that for $\xi = 10.3$. With the forecasting property of NGV interval observed, we find another metric in assisting the post-buckling behavior evaluation.

3.3 Polarization-selective NGV with varying initial shear modulus contrast

To consider the initial shear modulus contrast that effectively changes the transition region (Arora et al., 2022a), the variation of NGV interval with $k_\mu = 50$ and $k_\mu = 30$ are displayed in Fig. 4.

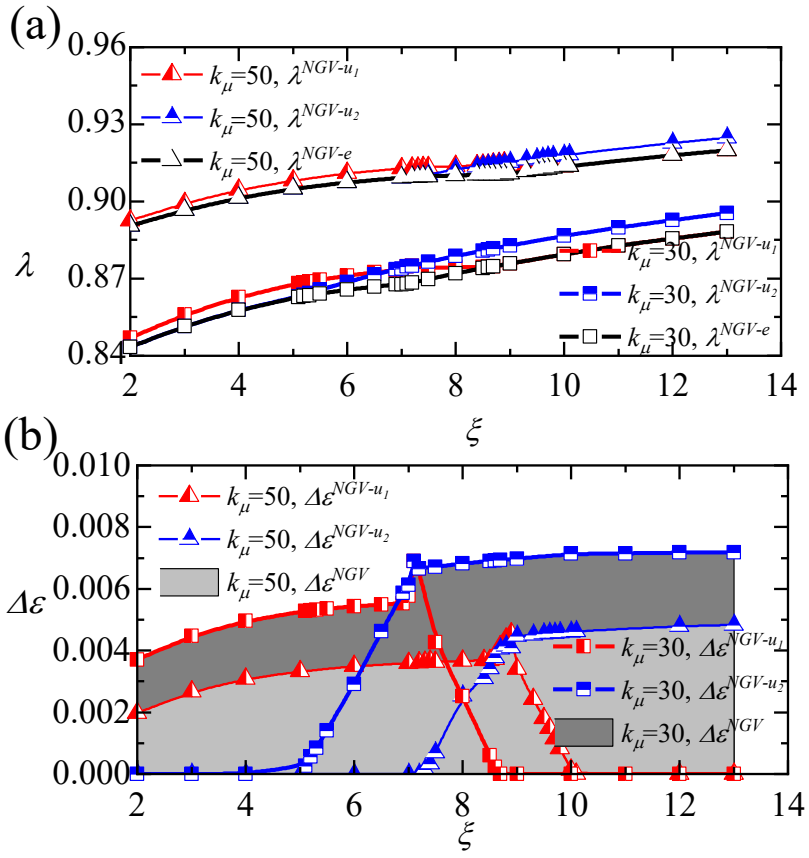

Fig. 4 NGV interval versus spacing ratio with $k_\mu = 50$ and $k_\mu = 30$. (a) The changes of λ^{NGV-u_1}, λ^{NGV-u_2}, and λ^{NGV-e}; (b) The variation of $\Delta\varepsilon^{NGV-u_1}$, $\Delta\varepsilon^{NGV-u_2}$, and $\Delta\varepsilon^{NGV}$. Volume fraction of fiber is set to be a constant $c^{(f)} = 0.05$.

The NGV intervals as the function of spacing ratio with $k_\mu = 50$ and $k_\mu = 30$ follow a similar pattern to those with $k_\mu = 80$. The transition of buckling direction from $\boldsymbol{e}_1$ to $\boldsymbol{e}_2$ is surrounded by a transition region, in which the NGV intervals evolve in an intriguing style. In this region, the total width shows an overall rising tendency with the spacing ratio. Outside of the transition region, the polarization of S-wave in NGV state is singly determined by the buckling direction. In the transition region, however, the spacing ratio under the transition point (represented by ξ_t) initially induces the NGV state for waves with u_1 polarization. When the spacing ratio is increasing, the onset stretch for u_2 and u_2 width is also rising. When $\xi > \xi_t$, u_1 width decreases to zero, leaving NGV state only for waves with u_2 polarization. In the vicinity of the transition point, both u_1 and u_2 widths increase simultaneously.

Remarkably, the decrease of the initial shear modulus contrast moves the transition point from $\xi_t = 10.2\ (k_\mu = 80)$ to $\xi_t = 8.9\ (k_\mu = 50)$ and eventually to $\xi_t = 7\ (k_\mu = 30)$. Furthermore, the interval, in which the NGV states for both polarizations appear, extends to $7.3 \le \xi \le 10.1$ with $k_\mu = 50$ and $5.1 \le \xi \le 8.6$ with $k_\mu = 30$. Consider a variable $\Delta\xi_d$ to denote the width of this NGV interval for both polarizations. It can be shown that $\Delta\xi_d$ increase from $1.5\ (k_\mu = 80)$ to $2.8\ (k_\mu = 50)$ and finally to $3.5\ (k_\mu = 30)$. Correspondingly, the transition region extends. As revealed(Arora et al., 2022b), the decrease in initial shear modulus contrast results in an increased NGV interval, say rising u_1, u_2, and total widths.

4 Conclusions

In summary, this paper studied the appearance of the negative group velocity state selectively active for S-waves with diverse polarizations propagating parallel to fibers in FC via numerical methods. By applying compression along the non-periodic (fiber) direction, NGV state can be activated on demand and tuned and tuned continuously with deformation.

We constructed a map of NGV intervals as a function of the spacing ratio/fiber arrangement. In most cases, NGV appears only for one polarization, aligned with the buckling direction predicted in instability analysis. However, in the transition region, collaborative tuning of spacing ratio and deformation enables a broad and controllable NGV states for both polarizations. These intervals occur sequentially with deformation, and initial polarization

shows NGV state is the predicted buckling direction. Notably, the shift from $\lambda^{NGV-u_1} > \lambda^{NGV-u_2}$ to $\lambda^{NGV-u_1} < \lambda^{NGV-u_2}$ versus spacing ratios highlights the transition point of buckling direction.

The forecast of NGV states can also be further shown by its correlation with post-buckling fiber morphologies. We observe that the appearance of NGV states for different polarizations mirrors the sequence of buckling directions. Meanwhile, the relative NGV interval width between polarizations correlates with the magnitude of the buckled fiber helix in the corresponding orientation. These findings suggest that the NGV state can serve as a predictive indicator in buckling analysis.

In our results, we observed the general trend of increasing NGV interval width along with narrowing spacing. Near the transition point, the interval width can nearly double compared to $\xi = 2$ across all shear modulus contrasts. Beyond this point, further increasing spacing yields limited additional gains (less than 0.001 in interval width). Reducing the shear modulus contrast from 80 to 50 results in an 87% increase in interval width, while reducing it further to 30 yields a more modest 25% increase. Considering the sensitivity of NGV states to deformation and practical limitations in material manufacturing processes, our results suggest searching for more controllable and experimentally viable soft composites with negative dispersion at moderate shear contrast and spacing ratios in the transition region.

Moreover, it can be possible to achieve NGV states in the absolute stable regime by leveraging matrix stiffening (Arora et al., 2022b). The control of light intensity during the 3D printing process (Wu et al., 2018; Xiang et al., 2020) applicably provides a viable tool in varying the molecular crosslink density (Treloar, 1975) of polymer chains and thus the matrix stiffening. In contrast to prior buckling NGV states, those in stable regions avoid the possibility of experiencing the structure switches and enable a wide NGV interval. The reported approach demonstrated the availability of diverse NGV states over a large design domain. This functionality could potentially be further applied in developing novel functionalities, such as the backward wave propagation as shown in electromagnetic (Loh et al., 2009; Siddiqui et al., 2003; Vashkovskii and Lokk, 2006) and optical systems (Feigenbaum et al., 2009).

Appendix A. Numerical Implementation

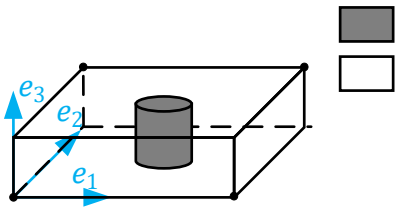

Fig. A-1 Unit cell for simulations. Point A is fixed.

The simulations are performed on COMSOL Multiphysics 5.5. The unit cell geometry is illustrated in Fig. A-1. The computational mesh is composed of Hexahedral elements swept along the fiber orientation.

The simulation follows a two-step procedure: first step is solving the finite deformation of the unit cell via the nonlinear Newton-Raphson method; second step is the evaluation of Bloch wave frequency and group velocity versus varying $\bar{K}_3$. With a custom search algorithm detecting the appearance of negative group velocity and checking the wave polarization, the bonds of NGV interval is determined. The boundary conditions applied in the first step are

$$\text{Step1.}\begin{cases} u_{1,right} = u_{1,left} + u_{1,C} \\ u_{2,right} = u_{2,left} \\ u_{3,right} = u_{3,left} \end{cases}, \begin{cases} u_{1,back} = u_{1,front} \\ u_{2,back} = u_{2,front} + u_{2,C}, \\ u_{3,back} = u_{3,front} \end{cases}$$
$$\begin{cases} u_{1,top} = u_{1,bottom} \\ u_{2,top} = u_{2,bottom} \\ u_{3,top} = u_{3,bottom} - \varepsilon H \end{cases}, \begin{cases} u_{1,A} = 0 \\ u_{2,A} = 0, \\ u_{3,A} = 0 \end{cases} \tag{A-1}$$

where ε is the deformation strain. The boundary conditions for the second step are

$$\text{Step2.}\begin{cases} u_{1,right} = u_{1,left} \\ u_{2,right} = u_{2,left} \\ u_{3,right} = u_{3,left} \end{cases}, \begin{cases} u_{1,back} = u_{1,front} \\ u_{2,back} = u_{2,front}, \\ u_{3,back} = u_{3,front} \end{cases}$$
$$\begin{cases} u_{1,top} = u_{1,bottom} e^{2\pi i \bar{K}_3/H} \\ u_{2,top} = u_{2,bottom} e^{2\pi i \bar{K}_3/H} \\ u_{3,top} = u_{3,bottom} e^{2\pi i \bar{K}_3/H} \end{cases}. \tag{A-2}$$

Acknowledgment

This research was performed using the compute resources and assistance of the UW-Madison Center For High Throughput Computing (CHTC) in the Department of Computer Sciences. The CHTC is supported by UW-Madison, the Advanced Computing Initiative, the Wisconsin Alumni Research Foundation, the Wisconsin Institutes for Discovery, and the National Science

Foundation, and is an active member of the OSG Consortium, which is supported by the National Science Foundation and the U.S. Department of Energys Office of Science. (Center for High Throughput Computing, 2006)

References

Arora, N., Li, J., Rudykh, S., 2022a. Tunable buckling configurations via in-plane periodicity in soft 3D-fiber composites: Simulations and experiments. Int. J. Solids Struct. 250, 111711. https://doi.org/10.1016/j.ijsolstr.2022.111711

Arora, N., Li, J., Slesarenko, V., Rudykh, S., 2020. Microscopic and longwave instabilities in 3D fiber composites with non-Gaussian hyperelastic phases. Int. J. Eng. Sci. 157. https://doi.org/10.1016/j.ijengsci.2020.103408

Arora, N., Yao, Q., Rudykh, S., 2022b. Deformation activated negative group velocity state in soft laminates. Extrem. Mech. Lett. 51. https://doi.org/10.1016/j.eml.2021.101592

Beauvois, K., Dawidowski, J., Fåk, B., Godfrin, H., Krotscheck, E., Ollivier, J., Sultan, A., 2018. Microscopic dynamics of superfluid 4He: A comprehensive study by inelastic neutron scattering. Phys. Rev. B 97, 184520. https://doi.org/10.1103/PhysRevB.97.184520

Bertoldi, K., Lopez-Pamies, O., 2012. Some remarks on the effect of interphases on the mechanical response and stability of fiber-reinforced elastomers. J. Appl. Mech. Trans. ASME 79, 031023. https://doi.org/10.1115/1.4006024

Bongard, F., Lissek, H., Mosig, J.R., 2010. Acoustic transmission line metamaterial with negative/zero/positive refractive index. Phys. Rev. B - Condens. Matter Mater. Phys. 82, 24–26. https://doi.org/10.1103/PhysRevB.82.094306

Carcaterra, A., Coppo, F., Mezzani, F., Pensalfini, S., 2019. Long-range retarded elastic metamaterials: wave-stopping, negative, and hypersonic or superluminal Group Velocity. Phys. Rev. Appl. 11, 1. https://doi.org/10.1103/PhysRevApplied.11.014041

Center for High Throughput Computing, 2006. Center for High Throughput Computing. https://doi.org/10.21231/GNT1-HW21

Chen, Y., Kadic, M., Wegener, M., 2021. Roton-like acoustical dispersion relations in 3D metamaterials. Nat. Commun. 12. https://doi.org/10.1038/s41467-021-23574-2

Cheng, Y., Yang, F., Xu, J.Y., Liu, X.J., 2008. A multilayer structured acoustic cloak with homogeneous isotropic materials. Appl. Phys. Lett. 92. https://doi.org/10.1063/1.2903500

Dorfmann, A., Ogden, R.W., 2010. Electroelastic waves in a finitely deformed electroactive material. IMA J. Appl. Math. (Institute Math. Its Appl. 75, 603–636.

https://doi.org/10.1093/imamat/hxq022

Feigenbaum, E., Kaminski, N., Orenstein, M., 2009. Negative dispersion: a backward wave or fast light? Nanoplasmonic examples. Opt. Express 17, 18934. https://doi.org/10.1364/OE.17.018934

Galich, P.I., Fang, N.X., Boyce, M.C., Rudykh, S., 2017a. Elastic wave propagation in finitely deformed layered materials. J. Mech. Phys. Solids 98, 390–410. https://doi.org/10.1016/j.jmps.2016.10.002

Galich, P.I., Rudykh, S., 2017. Shear wave propagation and band gaps in finitely deformed dielectric elastomer laminates: Long wave estimates and exact solution. J. Appl. Mech. Trans. ASME 84, 091002. https://doi.org/10.1115/1.4037159

Galich, P.I., Slesarenko, V., Li, J., Rudykh, S., 2018. Elastic instabilities and shear waves in hyperelastic composites with various periodic fiber arrangements. Int. J. Eng. Sci. 130, 51–61. https://doi.org/10.1016/j.ijengsci.2018.05.003

Galich, P.I., Slesarenko, V., Rudykh, S., 2017b. Shear wave propagation in finitely deformed 3D fiber-reinforced composites. Int. J. Solids Struct. 110–111, 294–304. https://doi.org/10.1016/j.ijsolstr.2016.12.007

Gao, N., Li, J., Bao, R.H., Chen, W.Q., 2019. Harnessing uniaxial tension to tune Poisson's ratio and wave propagation in soft porous phononic crystals: An experimental study. Soft Matter 15, 2921–2927. https://doi.org/10.1039/c8sm02468e

Gao, N., Qu, S., Li, J., Wang, J., Chen, W., 2021. Harnessing post-buckling deformation to tune sound absorption in soft Helmholtz absorbers. Int. J. Mech. Sci. 208, 106695. https://doi.org/10.1016/j.ijmecsci.2021.106695

García-Chocano, V.M., Christensen, J., Sánchez-Dehesa, J., 2014. Negative refraction and energy funneling by hyperbolic materials: An experimental demonstration in acoustics. Phys. Rev. Lett. 112, 11–15. https://doi.org/10.1103/PhysRevLett.112.144301

Geymonat, G., Müller, S., Triantafyllidis, N., 1993. Homogenization of nonlinearly elastic materials, microscopic bifurcation and macroscopic loss of rank-one convexity. Arch. Ration. Mech. Anal. 122, 231–290. https://doi.org/10.1007/BF00380256

Godfrin, H., Meschke, M., Lauter, H.-J., Sultan, A., Böhm, H.M., Krotscheck, E., Panholzer, M., 2012. Observation of a roton collective mode in a two-dimensional Fermi liquid.

Nature 483, 576–579. https://doi.org/10.1038/nature10919

Han, X., Liu, G.R., 2003. Elastic waves in a functionally graded piezoelectric cylinder. Smart Mater. Struct. 12, 962–971. https://doi.org/10.1088/0964-1726/12/6/014

Henshaw, D.G., Woods, A.D.B., 1961. Modes of Atomic Motions in Liquid Helium by Inelastic Scattering of Neutrons. Phys. Rev. 121, 1266–1274. https://doi.org/10.1103/PhysRev.121.1266

Kittel, C., 2005. Introduction to solid state physics. John Wiley \& sons, inc.

Lee, S.H., Wright, O.B., 2016. Origin of negative density and modulus in acoustic metamaterials. Phys. Rev. B 93, 1–14. https://doi.org/10.1103/PhysRevB.93.024302

Li, J., Slesarenko, V., Galich, P.I., Rudykh, S., 2018. Instabilities and pattern formations in 3D-printed deformable fiber composites. Compos. Part B Eng. 148, 114–122. https://doi.org/10.1016/j.compositesb.2018.04.049

Li, X.F., Ni, X., Feng, L., Lu, M.H., He, C., Chen, Y.F., 2011. Tunable unidirectional sound propagation through a sonic-crystal-based acoustic diode. Phys. Rev. Lett. 106, 1–4. https://doi.org/10.1103/PhysRevLett.106.084301

Loh, P.-R., Oskooi, A.F., Ibanescu, M., Skorobogatiy, M., Johnson, S.G., 2009. Fundamental relation between phase and group velocity, and application to the failure of perfectly matched layers in backward-wave structures. Phys. Rev. E 79, 065601. https://doi.org/10.1103/PhysRevE.79.065601

Mokhtari, A.A., Lu, Y., Srivastava, A., 2019. On the emergence of negative effective density and modulus in 2-phase phononic crystals. J. Mech. Phys. Solids 126, 256–271. https://doi.org/10.1016/j.jmps.2019.02.016

Rudykh, S., Debotton, G., 2012. Instabilities of hyperelastic fiber composites: Micromechanical versus numerical analyses. J. Elast. 106, 123–147. https://doi.org/10.1007/s10659-011-9313-x

Shan, S., Kang, S.H., Wang, P., Qu, C., Shian, S., Chen, E.R., Bertoldi, K., 2014. Harnessing multiple folding mechanisms in soft periodic structures for tunable control of elastic waves. Adv. Funct. Mater. 24, 4935–4942. https://doi.org/10.1002/adfm.201400665

Shmuel, G., Gei, M., Debotton, G., 2012. The Rayleigh-Lamb wave propagation in dielectric elastomer layers subjected to large deformations. Int. J. Non. Linear. Mech. 47, 307–316.

https://doi.org/10.1016/j.ijnonlinmec.2011.06.013

Siddiqui, O.F., Mojahedi, M., Eleftheriades, G. V, 2003. Periodically loaded transmission line with effective negative refractive index and negative group velocity. IEEE Trans. Antennas Propag. 51, 2619–2625. https://doi.org/10.1109/TAP.2003.817556

Slesarenko, V., Galich, P.I., Li, J., Fang, N.X., Rudykh, S., 2018. Foreshadowing elastic instabilities by negative group velocity in soft composites. Appl. Phys. Lett. 113. https://doi.org/10.1063/1.5042077

Smith, D.R., Pendry, J.B., Wiltshire, M.C.K., 2004. Metamaterials and negative refractive index. Science (80-.). 305, 788–792. https://doi.org/10.1126/science.1096796

Sun, H.X., Zhang, S.Y., Shui, X.J., 2012. A tunable acoustic diode made by a metal plate with periodical structure. Appl. Phys. Lett. 100. https://doi.org/10.1063/1.3693374

Treloar, L.R.G., 1975. The Physics of Rubber Elasticity. Oxford: Clarendon Press.

Triantafyllidis, N., Maker, B.N., 1985. On the comparison between microscopic and macroscopic instability mechanisms in a class of fiber-reinforced composites. J. Appl. Mech. Trans. ASME 52, 794–800. https://doi.org/10.1115/1.3169148

Vashkovskii, A. V., Lokk, E.H., 2006. Properties of backward electromagnetic waves and negative reflection in ferrite films. Uspekhi Fiz. Nauk 176, 403. https://doi.org/10.3367/UFNr.0176.200604d.0403

Wang, J., Allein, F., Boechler, N., Friend, J., Vazquez-Mena, O., 2021. Design and fabrication of negative-refractive-index metamaterial unit cells for near-megahertz enhanced acoustic transmission in biomedical ultrasound applications. Phys. Rev. Appl. 15, 1. https://doi.org/10.1103/PhysRevApplied.15.024025

Wang, K., Chen, Y., Kadic, M., Wang, C., Wegener, M., 2022. Nonlocal interaction engineering of 2D roton-like dispersion relations in acoustic and mechanical metamaterials. Commun. Mater. 3, 35. https://doi.org/10.1038/s43246-022-00257-z

Wang, K., Schneider, J.L.G., Chen, Y., Iglesias Martínez, J.A., Kadic, M., Wang, C., 2026. Roton dispersion and displacement oscillatory for a nonlocal mechanical system. Eur. J. Mech. - A/Solids 115, 105842. https://doi.org/10.1016/j.euromechsol.2025.105842

Wang, P., Casadei, F., Shan, S., Weaver, J.C., Bertoldi, K., 2014. Harnessing buckling to design tunable locally resonant acoustic metamaterials. Phys. Rev. Lett. 113, 1–5.

https://doi.org/10.1103/PhysRevLett.113.014301

Woods, A.D.B., 1965. Neutron Inelastic Scattering from Liquid Helium at Small Momentum Transfers. Phys. Rev. Lett. 14, 355–356. https://doi.org/10.1103/PhysRevLett.14.355

Wu, J., Zhao, Z., Hamel, C.M., Mu, X., Kuang, X., Guo, Z., Qi, H.J., 2018. Evolution of material properties during free radical photopolymerization. J. Mech. Phys. Solids 112, 25–49. https://doi.org/10.1016/j.jmps.2017.11.018

Xiang, Y., Schilling, C., Arora, N., Boydston, A.J., Rudykh, S., 2020. Mechanical characterization and constitutive modeling of visco-hyperelasticity of photocured polymers. Addit. Manuf. 36, 101511. https://doi.org/10.1016/j.addma.2020.101511

Yerrapragada, K., Yang, H., Lee, W., Eriten, M., 2023. Characterization of drying-induced changes in moduli and internal stresses in a constrained gel using laser vibrometry. Soft Matter 20, 813–822. https://doi.org/10.1039/d3sm01328f

Zhang, G.Y., Gao, X.L., Ding, S.R., 2018. Band gaps for wave propagation in 2-D periodic composite structures incorporating microstructure effects. Acta Mech. 229, 4199–4214. https://doi.org/10.1007/s00707-018-2207-2

Zhu, R., Liu, X.N., Hu, G.K., Sun, C.T., Huang, G.L., 2014. Negative refraction of elastic waves at the deep-subwavelength scale in a single-phase metamaterial. Nat. Commun. 5, 5510. https://doi.org/10.1038/ncomms6510